

# Thermo-electric effects in an anisotropic active strain electromechanical model

CHRISTIAN CHERUBINI<sup>\*,†</sup>, SIMONETTA FILIPPI<sup>\*,†</sup>, ALESSIO GIZZI<sup>\*</sup>,  
ALESSANDRO LOPPINI<sup>\*</sup>, RICARDO RUIZ BAIER<sup>‡</sup>

March 15, 2018

## Abstract

In this paper we introduce a new mathematical model for the active contraction of the cardiac muscle under different thermo-electric and nonlinear conductivity properties. The passive hyperelastic response of the tissue is described by an orthotropic exponential model, whereas the ionic activity dictates active contraction incorporated through the concept of orthotropic active strain. We use a fully incompressible formulation, and the generated strain modifies directly the conductivity mechanisms in the medium through the pull-back transformation. We also investigate the influence of thermo-electric effects in the onset of multiphysics emergent spatiotemporal dynamics, using nonlinear diffusion. It turns out that these ingredients have a key role in reproducing pathological rhythms such as ventricular fibrillation, during inflammatory events, for instance. The specific structure of the governing equations (written in terms of Kirchhoff stress, displacements, solid pressure, electric potential, activation generation, and ionic variables) suggests to cast the problem in mixed-primal form, and to use a mixed-primal finite element method for its numerical approximation. We finally explore the properties of the model, together with the importance of coupling variables, by means of a few computational experiments.

**Key words:** Cardiac electromechanics, Anisotropic active strain, Thermo-electric coupling, Spiral and scroll wave propagation, Numerical simulations.

## 1 Introduction

Temperature variations may have a direct impact on many of the fundamental mechanisms in the cardiac function [57]. Substantial differences have been reported in the conduction velocity and spiral drift of chaotic electric potential propagation in a number of modelling and computationally-oriented studies [2, 19, 20, 25], and several experimental tests confirm that this is the case not only for cardiac tissue, but for other excitable systems [24, 33]. The phenomenon is however not restricted to electrochemical interactions, but it also might involve mechanical properties [26, 36, 52]. The cardiac muscle is quite sensitive to mechanical stimulation, and the modification of deformation patterns can be very susceptible to external agents such as temperature. For instance, enhanced tissue heterogeneities can be observed when the medium is exposed to altered thermal states, and in turn these can give rise to irregular mechano-chemical dynamics. Our goal is to investigate the role of the aforementioned effects

---

<sup>\*</sup>Nonlinear Physics and Mathematical Modeling, Department of Engineering, University Campus Bio-Medico, Rome, Italy. E-mail: {c.cherubini,s.filippi,a.gizzi,a.loppini}@unicampus.it.

<sup>†</sup>International Center for Relativistic Astrophysics (ICRA), and ICRANet, Piazza delle Repubblica 10, I-65122 Pescara, Italy.

<sup>‡</sup>Corresponding author. Mathematical Institute, University of Oxford, A. Wiles Building, Woodstock Road, Oxford OX2 6GG, UK. E-mail: ruizbaier@maths.ox.ac.uk.

in the development and sustainability of cardiac arrhythmias. These complex emerging phenomena originate from multifactorial and multiphysical interactions [32, 45], and they are responsible for a large amount of cases of pathological dysfunction and casualties. The model we propose here has therefore potential in the investigation of some mechanisms provoking such complex dynamics, in particular those arising during atrial and ventricular fibrillation.

Our modelling framework is constructed using the temperature-based two-variable phenomenological model from [25], which also includes a nonlinear conductivity representing a more general diffusion mechanism. We postulate then an extended model that also accounts for active deformation of the tissue, where the specific form of the electromechanical coupling is dictated by the orthotropic active strain framework proposed in [48].

Even if computational models for the electromechanics of the heart are increasingly complex and account for many multiphysics and multiscale effects (see e.g. 11, 12, 23, 37, 54 and the review paper 46), we are only aware of one recent study [10] that addresses similar questions to the ones analysed here. However that study is restricted to one-dimensional domains, it uses the two-variable model from [41], and it assumes an active stress approach for a simplified neo-Hookean material in the absence of an explicit stretch state.

## 2 A new model for thermo-electric active strain

In this section we provide an abridged derivation of the set of partial differential equations describing the multiscale coupling between electric, thermal, mechanical, and ionic processes valid for excitable, deformable media.

### 2.1 Muscle contraction via the active strain approach

Let  $\Omega \subset \mathbb{R}^d$ ,  $d \in \{2, 3\}$  denote a deformable body with piecewise smooth boundary  $\partial\Omega$ , regarded in its reference configuration, and denote by  $\boldsymbol{\nu}$  the outward unit normal vector on  $\partial\Omega$ . The kinematical description of finite deformations regarded on a time interval  $t \in (0, t_{\text{final}}]$  is made precise as follows. A material point in  $\Omega$  is denoted by  $\boldsymbol{x}$ , whereas  $\boldsymbol{u}(t) : \Omega \rightarrow \mathbb{R}^d$  will denote the displacement field defining its new position  $\boldsymbol{x}_t$  within the body  $\Omega_t$  in the current, deformed configuration. The tensor  $\mathbf{F} := \nabla \boldsymbol{u}$  is the gradient (applied with respect to the fixed material coordinates) of the deformation map; its Jacobian determinant, denoted by  $J = \det \mathbf{F}$ , measures the solid volume change during the deformation; and  $\mathbf{C} = \mathbf{F}^\top \mathbf{F}$  is the right Cauchy-Green deformation tensor on which all strain measures will be based (here the superscript  $(\ )^\top$  denotes the transpose operator). The first isotropic invariant ruling deviatoric effects is  $I_1(\mathbf{C}) = \text{tr } \mathbf{C}$ , and for generic unitary vectors  $\boldsymbol{f}_0, \boldsymbol{s}_0$ , the scalars  $I_{4,f}(\mathbf{C}) = \boldsymbol{f}_0 \cdot (\mathbf{C}\boldsymbol{f}_0)$ ,  $I_{8,fs}(\mathbf{C}) = \boldsymbol{f}_0 \cdot (\mathbf{C}\boldsymbol{s}_0)$  are direction-dependent pseudo-invariants of  $\mathbf{C}$  measuring fibre-aligned stretch (see e.g. 51). As usual,  $\mathbf{I}$  denotes the  $d \times d$  identity tensor. In the remainder of the presentation we will restrict all space differential operators to the material coordinates.

Next we recall the active strain model for ventricular electromechanics as introduced in [42]. There, the contraction of the tissue results from activation mechanisms governed by internal variables and incorporated into the finite elasticity context using a virtual multiplicative decomposition of the deformation gradient into a passive (purely elastic) and an active part  $\mathbf{F} = \mathbf{F}_E \mathbf{F}_A$ , with

$$\mathbf{F}_A = \mathbf{I} + \gamma_f \boldsymbol{f}_0(\boldsymbol{x}) \otimes \boldsymbol{f}_0(\boldsymbol{x}) + \gamma_s \boldsymbol{s}_0(\boldsymbol{x}) \otimes \boldsymbol{s}_0(\boldsymbol{x}) + \gamma_n \boldsymbol{n}_0(\boldsymbol{x}) \otimes \boldsymbol{n}_0(\boldsymbol{x}).$$

The coefficients  $\gamma_i$ , with  $i = f, s, n$ , are smooth scalar functions encoding the macroscopic stretch in specific directions, whose precise definition will be postponed to Section 2.3. The inelastic contribution to the deformation modifies the size and orientation of the cardiac fibres, and then compatibility of the motion is restored through an elastic deformation accommodating the active strain distortion. The triplet  $(\boldsymbol{f}_0(\boldsymbol{x}), \boldsymbol{s}_0(\boldsymbol{x}), \boldsymbol{n}_0(\boldsymbol{x}))$  represents a coordinate system pointing in the local direction of cardiac

fibres, transversal sheetlet compound, and normal cross-fibre direction  $\mathbf{n}_0(\mathbf{x}) = \mathbf{f}_0(\mathbf{x}) \times \mathbf{s}_0(\mathbf{x})$ . Note that the system is restricted to  $(\mathbf{f}_0(\mathbf{x}), \mathbf{s}_0(\mathbf{x}))$  in the two-dimensional case. Constitutive relations defining the material properties and underlying microstructure of the myocardial tissue will follow the orthotropic model proposed in [27], for which the strain energy function and the first Piola-Kirchhoff stress tensor (after applying the active strain decomposition) read respectively (see details in 49)

$$\Psi(\mathbf{F}_E) = \frac{a}{2b} e^{b(I_1^E - d)} + \frac{a_{fs}}{2b_{fs}} [e^{b_{fs}(I_{8,fs}^E)^2} - 1] + \sum_{i \in \{f, s\}} \frac{a_i}{2b_i} [e^{b_i(I_{4,i}^E - 1)_+^2} - 1], \quad \mathbf{P} = \frac{\partial \Psi}{\partial \mathbf{F}} - p \mathbf{J} \mathbf{F}^{-t}, \quad (2.1)$$

where  $a, b, a_i, b_i$  with  $i \in \{f, s, fs\}$  are material parameters,  $p$  denotes the solid hydrostatic pressure, and we have used the notation  $(s)_+ := s$  if  $s > 0$  or zero otherwise. Switching off the anisotropic contributions under compression ensures that the associated terms in the strain energy function (in both the pure passive and active-strain formulations) are strongly elliptic [44]. The modified elastic invariants  $I_i^E$  are functions of the coefficients  $\gamma_i$  and the invariant and pseudo invariants as follows

$$I_1^E = \left[ 1 - \frac{\gamma_n(\gamma_n + 2)}{(\gamma_n + 1)^2} \right] I_1 + \left[ \gamma_n \frac{\gamma_n + 2}{(\gamma_n + 1)^2} - \gamma_f \frac{\gamma_f + 2}{(\gamma_f + 1)^2} \right] I_{4,f} + \left[ \gamma_n \frac{\gamma_n + 2}{(\gamma_n + 1)^2} - \gamma_s \frac{\gamma_s + 2}{(\gamma_s + 1)^2} \right] I_{4,s},$$

$$I_{4,f}^E = \frac{I_{4,f}}{(\gamma_f + 1)^2}, \quad I_{4,s}^E = \frac{I_{4,s}}{(\gamma_s + 1)^2}, \quad I_{8,fs}^E = \frac{I_{8,fs}}{(\gamma_f + 1)(\gamma_s + 1)}.$$

Accordingly, the active strain and consequently the force associated to the active part of the total stress, will receive contributions acting on the three main directions.

The balance of linear momentum together with the incompressibility constraint are written, when posed in the inertial reference frame and under pseudo-static mechanical equilibrium, in the following way

$$-\nabla \cdot \mathbf{P} = \rho_0 \mathbf{b} \quad \text{in } \Omega \times (0, t_{\text{final}}], \quad (2.2a)$$

$$\rho J - \rho_0 = 0 \quad \text{in } \Omega \times (0, t_{\text{final}}], \quad (2.2b)$$

where  $\rho_0, \rho$  are the reference and current medium density, and  $\mathbf{b}$  is a vector of body loads. The balance of angular momentum translates into the condition of symmetry of the Kirchhoff stress tensor  $\mathbf{\Pi} = \mathbf{P} \mathbf{F}^t$ , which is in turn encoded into the momentum and constitutive relations (2.2a), (2.1).

Defining  $\mathcal{G}(\mathbf{u}) := \frac{\partial \Psi}{\partial \mathbf{F}} \mathbf{F}^t$  we then have

$$\mathbf{\Pi} = \mathcal{G}(\mathbf{u}) - p \mathbf{J} \mathbf{I}. \quad (2.3)$$

## 2.2 A modified Karma model for cardiac action potential

Let us denote by  $I_{\text{ext}}$  a spatio-temporal external stimulus applied to the medium. On the undeformed configuration we proceed to write the following monodomain equations describing the transmembrane potential propagation and the dynamics of slow recovery currents according to a specific temperature  $T$ :

$$\frac{\partial v}{\partial t} - \nabla \cdot [\mathbf{D}(v, \mathbf{F}) \nabla v] = \frac{f(v, n)}{\tau_v(T)} + I_{\text{ext}} \quad \text{in } \Omega \times (0, t_{\text{final}}], \quad (2.4a)$$

$$\frac{dn}{dt} = \frac{g(v, n)}{\tau_n(T)} \quad \text{in } \Omega \times (0, t_{\text{final}}]. \quad (2.4b)$$

This reaction-diffusion system is endowed with the following specifications, taking the membrane model proposed in [31], and adapting it to include thermo-electric effects following [19, 25]

$$f(v, n) := -v + [v^* - \mathcal{S}(n)][1 - \tanh(v - v_*)] \frac{v^2}{2}, \quad (2.5a)$$

$$g(v, n) := \mathcal{R}(n)\mathcal{H}(v - v_n) - [1 - \mathcal{H}(v - v_n)]n, \quad (2.5b)$$

$$\mathcal{R}(n) := \frac{1 - (1 - e^{-L})n}{1 - e^{-L}}, \quad \mathcal{S}(n) := n^M, \quad (2.5c)$$

$$\tau_v(T) := \frac{\tau_v^0}{1 + \beta(T - T_0)}, \quad \tau_n(T) := \tau_n^0 Q_{10}^{-(T - T_0)/10}. \quad (2.5d)$$

Here  $\mathcal{H}(x)$  stands for the Heaviside step function (i.e.  $\mathcal{H}(s) = 0$  for  $s \leq 0$  and  $\mathcal{H}(s) = 1$  for  $s > 0$ ), the normalised transmembrane voltage assumes values in  $[0, 1]$ , and the resting state of the dynamical system is  $(v, n) = (0, 0)$ . The function  $\mathcal{R}(n)$  modulates the time-frame between the end of an action potential pulse and the beginning of the next one (diastolic interval) and the duration of the subsequent action potential pulse. The dispersion map  $\mathcal{S}(n)$  relates the instantaneous speed of the action potential front-end at a given spatial point, with the time elapsed since the back-end of a previous pulse that has passed through the same location. In turn, these functions are tuned by the parameters  $L, M$ , respectively. In (2.5d), an Arrhenius exponential law modifies the dynamics of the gating variable, whereas the so-called Moore term defines the time constant  $\tau_v(T)$  associated to the transmembrane voltage.

We observe that due to the Piola transformation (forcing a compliance of the diffusion tensor using the deformation gradients), the conductivity tensor  $\mathbf{D}(\cdot, \cdot)$  in (2.4a) depends nonlinearly on the deformation gradient, whereas self-diffusion is here taken as the potential-dependent diffusivity proposed in [25], but appropriately modified to incorporate information about preferred directions of diffusivity according to the microstructure of the tissue. More precisely, we set

$$\mathbf{D}(v, \mathbf{F}) = [D_0/2 + D_1v + D_2v^2]J\mathbf{C}^{-1} + D_0/2J\mathbf{F}^{-1}\mathbf{f}_0 \otimes \mathbf{f}_0\mathbf{F}^{-T}, \quad (2.6)$$

where the values taken by the parameters  $D_i$ ,  $i = 0, 1, 2$  (as well as all remaining model constants) are displayed in Table 4.1, below. Note that here the diffusivity is mainly affected by the fibre-to-fibre connections, and the presence of  $J\mathbf{C}^{-1}$  suggests a strain-enhanced tissue conductivity, also referred to as geometric feedback [11]. The constants  $D_1, D_2$  encode the effect of linear and quadratic self-diffusion, and they have special importance at the depolarisation plateau phase, since they modify the speed and wavelength of the propagating waves. We also note that even for resting transmembrane potential, the conductivity tensor remains positive definite (see also 29 for an alternative approach).

### 2.3 Activation mechanisms

A constitutive equation for the activation functions  $\gamma_i$  in terms of the microscopic cell shortening  $\xi$  is as follows [48]

$$\gamma_f(\xi) = \xi, \quad \gamma_s(\xi) = (1 + \xi)^{-1}(1 + K_0\xi)^{-1} - 1, \quad \gamma_n(\xi) = K_0\xi, \quad (2.7)$$

and the specific relation between the myocyte shortening  $\xi$  and the dynamics of slow ionic quantities (in the context of our phenomenological model, only  $n$ ) is made precise using the law

$$\frac{d\xi}{dt} = \frac{\ell(\xi, n)}{\tau_\xi(T)} \quad \text{in } \Omega \times (0, t_{\text{final}}], \quad (2.8)$$

where, in analogy to (2.5), the dynamics of the myocyte shortening are here additionally modulated by a temperature-dependent constant

$$\ell(\xi, n) := K_1\xi(1 + n)^{-1} - K_2\xi^2n, \quad \tau_\xi(T) := \tau_\xi^0 Q_{10}^{-(T - T_0)/25}. \quad (2.9)$$

The structure of (2.8) suggests that thermo-electric effects can be straightforwardly incorporated in other models for cellular activation (depending on cross-bridge transitions [35], on calcium - stretch rate couplings in a viscoelastic setting [18], or using phenomenological descriptions), simply through a rescaling with  $\tau_\xi$ .

## 2.4 Initial and boundary conditions

Equations (2.2a)-(2.2b) will be supplemented either with mixed normal displacement-traction boundary conditions

$$\mathbf{u} \cdot \boldsymbol{\nu} = 0 \quad \text{on} \quad \partial\Omega_D \times (0, t_{\text{final}}], \quad \text{and} \quad \mathbf{P}\boldsymbol{\nu} = p_N J \mathbf{F}^{-\text{t}} \boldsymbol{\nu} \quad \text{on} \quad \partial\Omega_N \times (0, t_{\text{final}}], \quad (2.10)$$

(where  $\partial\Omega_D, \partial\Omega_N$  conform a disjoint partition of the boundary, the traction written in terms of the first Piola-Kirchhoff stress tensor is  $\mathbf{t} = \mathbf{P}\boldsymbol{\nu}$ , and the term  $p_N$  denotes a possibly time-dependent prescribed boundary pressure), or alternatively with Robin conditions on the whole boundary

$$\mathbf{P}\boldsymbol{\nu} + \eta J \mathbf{F}^{-\text{t}} \mathbf{u} = \mathbf{0} \quad \text{on} \quad \partial\Omega \times (0, t_{\text{final}}], \quad (2.11)$$

which account for stiff springs connecting the cardiac medium with the surrounding soft tissue and organs (whose stiffness is encoded in the scalar  $\eta$ ). On the other hand, for the nonlinear diffusion equation (2.4a) we prescribe zero-flux boundary conditions representing insulated tissue (see 7 for an extended discussion)

$$\mathbf{D}(v, \mathbf{F}) \nabla v \cdot \boldsymbol{\nu} = 0 \quad \text{on} \quad \partial\Omega \times (0, t_{\text{final}}]. \quad (2.12)$$

Finally, the coupled set of equations is closed after defining adequate initial data for the transmembrane potential and for the internal variables  $\xi, n$ :

$$v(\mathbf{x}, 0) = v_0(\mathbf{x}), \quad n(\mathbf{x}, 0) = n_0(\mathbf{x}), \quad \xi(\mathbf{x}, 0) = \xi_0(\mathbf{x}) \quad \text{on} \quad \Omega \times \{0\}. \quad (2.13)$$

For the electrical model we chose resting values for the transmembrane potential and for the slow recovery  $v_0 = n_0 = 0$ , where initiation of wave propagation will be induced with S1-S2-type protocols. A non-zero initial value  $\xi_0 = 0.001$  is considered for the myocyte shortening.

## 3 Galerkin finite element method

### 3.1 Mixed-primal formulation in weak form

The specific structure of the governing equations (written in terms of the Kirchhoff stress, displacements, solid pressure, electric potential, activation generation, and ionic variables) suggests to cast the problem in mixed-primal form, that is, setting the active mechanical problem using a three-field formulation, and a primal form for the equations driving the electrophysiology. Further details on similar derivations can be found in [50] (see also 4, 5 for nearly incompressible hyperelasticity problems). Restricting to the case of Robin boundary data for the mechanical problem, we proceed to test (2.2a), (2.2b), (2.3) against adequate functions, and doing so also for (2.4) yields the problem: For  $t > 0$ , find  $(\boldsymbol{\Pi}, \mathbf{u}, p) \in \mathbb{H}(\mathbf{div} \Omega) \times \mathbf{H}^1(\Omega) \times L^2(\Omega)$  and  $(v, n, \xi) \in \mathbf{H}^1(\Omega)^3$  such that

$$\int_{\Omega} [\boldsymbol{\Pi} - \mathcal{G}(\mathbf{u}) + pJ] : \boldsymbol{\tau} = 0 \quad \forall \boldsymbol{\tau} \in \mathbb{H}(\mathbf{div} \Omega), \quad (3.1a)$$

$$\int_{\Omega} \boldsymbol{\Pi} : \nabla \mathbf{v} \mathbf{F}^{-\text{t}} - \int_{\partial\Omega} \eta \mathbf{F}^{-\text{t}} \mathbf{u} \cdot \mathbf{v} = \int_{\Omega} \rho_0 \mathbf{b} \cdot \mathbf{v} \quad \forall \mathbf{v} \in \mathbf{H}^1(\Omega), \quad (3.1b)$$

$$\int_{\Omega} [J - 1]q = 0 \quad \forall q \in L^2(\Omega), \quad (3.1c)$$

$$\int_{\Omega} \frac{\partial v}{\partial t} w + \int_{\Omega} \mathbf{D}(v, \mathbf{F}) \nabla v \cdot \nabla w = \int_{\Omega} \left[ \frac{f(v, n)}{\tau_v(T)} + I_{\text{ext}} \right] w \quad \forall w \in \mathbf{H}^1(\Omega), \quad (3.1d)$$

$$\int_{\Omega} \left( \frac{\partial n}{\partial t} m + \frac{\partial \xi}{\partial t} \varphi \right) = \int_{\Omega} \left( \frac{g(v, n)}{\tau_n(T)} m + \frac{\ell(\xi, n)}{\tau_{\xi}(T)} \varphi \right) \quad \forall (m, \varphi) \in \mathbf{H}^1(\Omega)^2. \quad (3.1e)$$

### 3.2 Galerkin discretisation

The spatial discretisation follows a mixed-primal Galerkin approach based on the formulation (3.1). Let us denote by  $\mathcal{T}_h$  a regular partition of  $\Omega$  into tetrahedra  $K$  of maximum diameter  $h_K$ , and define the meshsize as  $h := \max\{h_K : K \in \mathcal{T}_h\}$ . The specific finite element method we chose here is based on solving the discrete weak form of the hyperelasticity equations using Raviart-Thomas elements of first order to approximate rows of the stress tensor, piecewise linear approximation of displacements, and piecewise constant approximation of solid pressure. All unknowns in the electrophysiology are discretised with Lagrange finite elements (piecewise linear and continuous functions). More precisely, we use the finite dimensional spaces  $\mathbb{H}_h \subset \mathbb{H}(\mathbf{div}; \Omega)$ ,  $\mathbf{V}_h \subset \mathbf{H}^1(\Omega)$ ,  $W_h \subset H^1(\Omega)$ ,  $Q_h \subset L^2(\Omega)$  defined as follows:

$$\begin{aligned}\mathbb{H}_h &:= \{\boldsymbol{\tau}_h \in \mathbb{H}(\mathbf{div}; \Omega) : (\tau_h^{i1}, \dots, \tau_h^{id})^\top \in \mathbb{RT}_k(K), \forall i \in \{1, \dots, d\}, \forall K \in \mathcal{T}_h\}, \\ \mathbf{V}_h &:= \{\mathbf{v}_h \in \mathbf{H}^1(\Omega) : \mathbf{v}_h|_K \in \mathbb{P}_{k+1}(K)^d, \forall K \in \mathcal{T}_h\}, \\ Q_h &:= \{q_h \in L^2(\Omega) : q_h|_K \in \mathbb{P}_k(K), \forall K \in \mathcal{T}_h\}, \\ W_h &:= \{w_h \in H^1(\Omega) : w_h|_K \in \mathbb{P}_{k+1}(K), \forall K \in \mathcal{T}_h\},\end{aligned}$$

where  $\mathbb{P}_r(R)$  denotes the space of polynomial functions of degree  $s \leq r$  defined on the set  $R$ , and  $\mathbb{RT}_k(K) = \mathbb{P}_k(K)^d \oplus \mathbb{P}_k(K)\mathbf{x}$  represents the Raviart-Thomas space of order  $k \geq 0$ , defined locally on each tetrahedral element  $K \in \mathcal{T}_h$  [21]. Assuming zero body loads, and applying a backward Euler time integration we end up with the following fully-discrete nonlinear electromechanical problem, starting from the discrete initial data  $v_h^0, n_h^0, \xi_h^0$ . For each  $j = 0, 1, \dots$ : find  $(\boldsymbol{\Pi}_h^{j+1}, \mathbf{u}_h^{j+1}, p_h^{j+1})$  and  $(v_h^{j+1}, n_h^{j+1}, \xi_h^{j+1})$  such that

$$\begin{aligned}\int_{\Omega} [\boldsymbol{\Pi}_h^{j+1} - \mathcal{G}(\mathbf{u}_h^{j+1}) + p_h^{j+1} J(\mathbf{u}_h^{j+1})] : \boldsymbol{\tau}_h &= 0 & \forall \boldsymbol{\tau}_h \in \mathbb{H}_h, \\ \int_{\Omega} \boldsymbol{\Pi}_h^{j+1} : \nabla \mathbf{v}_h \mathbf{F}^{-\top}(\mathbf{u}_h^{j+1}) - \int_{\partial\Omega} \eta \mathbf{F}^{-\top}(\mathbf{u}_h^{j+1}) \mathbf{u}_h^{j+1} \cdot \mathbf{v}_h &= 0 & \forall \mathbf{v}_h \in \mathbf{V}_h, \\ \int_{\Omega} [J(\mathbf{u}_h^{j+1}) - 1] q_h &= 0 & \forall q_h \in Q_h, \\ \int_{\Omega} \frac{v_h^{j+1} - v_h^j}{\Delta t} w_h + \int_{\Omega} \mathbf{D}(v_h^{j+1}, \mathbf{F}(\mathbf{u}_h^{j+1})) \nabla v_h^{j+1} \cdot \nabla w_h - \int_{\Omega} \left[ \frac{f(v_h^{j+1}, n_h^{j+1})}{\tau_v(T)} + I_{\text{ext}} \right] w_h &= 0 & \forall w_h \in W_h, \\ \int_{\Omega} \frac{n_h^{j+1} - n_h^j}{\Delta t} m_h - \int_{\Omega} \frac{g(v_h^{j+1}, n_h^{j+1})}{\tau_n(T)} m_h &= 0 & \forall m_h \in W_h, \\ \int_{\Omega} \frac{\xi_h^{j+1} - \xi_h^j}{\Delta t} \varphi_h - \int_{\Omega} \frac{\ell(\xi_h^{j+1}, n_h^{j+1})}{\tau_{\xi}(T)} \varphi_h &= 0 & \forall \varphi_h \in W_h.\end{aligned}$$

### 3.3 Implementation details

The coupling between activated mechanics and the electrophysiology solvers is not done monolithically, but rather realised using a segregated fixed-point scheme. The nonlinear mechanics are solved using an embedded Newton-Raphson method and an operator splitting algorithm separates an implicit diffusion solution (where another Newton iteration handles the nonlinear self-diffusion) from an explicit reaction step for the kinetic equations, turning the overall solver into a semi-implicit method. Updating and storing of the internal variables  $\xi$  and  $n$  is done locally at the quadrature points. The routines are implemented using the finite element library FEniCS [1], and in all cases the solution of linear systems is carried out with the BiCGStab method preconditioned with an algebraic multigrid solver. The domains to be studied consist of 3D slabs and ellipsoidal geometries, discretised into tetrahedral meshes of maximum meshsize  $h = 0.01$  cm. The time discretisation uses a fixed timestep of  $\Delta t = 0.05$  ms (dictated by the dynamics of the cell ionic model rather than by a CFL condition, as the diffusion is discretised implicitly), and we observe that the hyperelasticity equations have a different inherent timescale, so we update their solution every five steps taken by the electrophysiology solver. Since

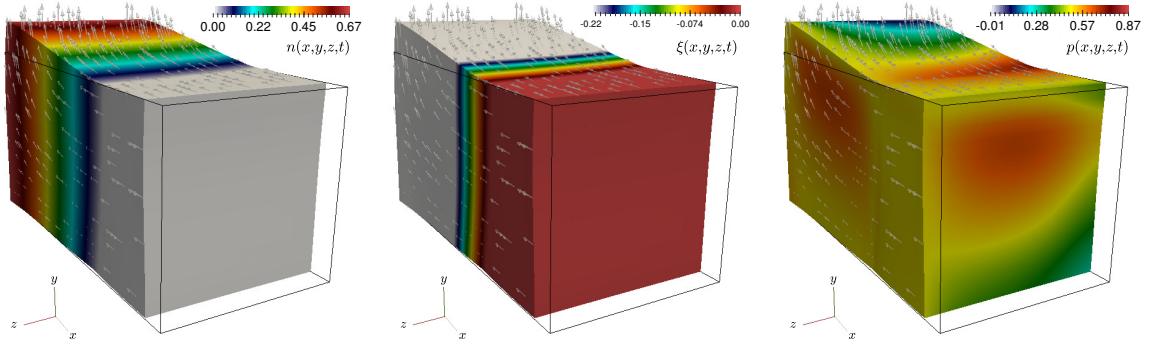


Figure 4.1: Samples of the approximate solution (recovery variable, cell shortening, and solid pressure) produced after two cycles, at  $t = 120$  ms. For this plot we have used  $T = 39^\circ\text{C}$  and the fields are portrayed on the deformed configuration, where the arrows indicate the direction of displacement.

in (2.8) the evolution of myocyte shortening does not depend locally on the macroscopic stretch, the activation system can be conveniently solved together with the ionic model. A tolerance of  $1e-7$  on the  $\ell^\infty$ -norm of the residual is employed to terminate the Newton iterates.

## 4 Numerical results

Table 4.1: Model parameters for the electromechanical model (2.2), (2.4), (2.8). Values are taken from [9, 19, 27, 48].

$a = 0.333$ [kPa]	$a_f = 18.535$ [kPa]	$a_s = 2.564$ [kPa]	$a_{fs} = 0.417$ [-]
$b = 9.242$ [-]	$b_f = 15.972$ [-]	$b_s = 10.446$ [-]	$b_{fs} = 11.602$ [-]
$v_\star = 3$ [-]	$v_n = 1$ [-]	$v^\star = 1.5415$ [-]	$Q_{10} = 1.5$ [-]
$\tau_v = 2.5$ [ms]	$\beta = 0.008$ [-]	$\tau_n = 250$ [ms]	$D_0 = 0.85$ [ $\text{cm}^2/\text{s}$ ]
$D_1 = 0.09$ [ $\text{cm}^2/\text{s}$ ]	$D_2 = 0.01$ [ $\text{cm}^2/\text{s}$ ]	$L = 0.9$ [-]	$M = 9$ [-]
$K_0 = 5$ [-]	$K_1 = 0.45$ [-]	$K_2 = 6.22$ [-]	$\eta \in \{0.05, 0.9\}$ [kPa]

### 4.1 Conduction velocity assessment

We consider the electromechanical model (2.2), (2.4), (2.8) defined on the 3D slab  $\Omega = (0, 6.72) \times (0, 3.36) \times (0, 3.36)$ . The boundary conditions correspond to (2.10) and (2.12). The bottom ( $z = 0$ ), back ( $y = 0$ ), and left ( $x = 0$ ) sides of the block will constitute  $\partial\Omega_D$  where we impose zero normal displacements, and on the remainder of the boundary  $\partial\Omega_N = \partial\Omega \setminus \partial\Omega_D$  we prescribe zero traction. A stimulus of amplitude 3 and duration 3ms is applied on the left wall at time  $t = 1$  ms, which initiates a planar wave propagation. At  $T = 37^\circ\text{C}$  the thermo-electric effects are turned off (both  $Q_{10}$  and Moore terms equal 1), and the reported maximum conduction velocity of 30 cm/s can be computed using  $\tilde{D} = 1.1 \text{ cm}^2/\text{s}$  (that is, setting  $D_1 = D_2 = 0$ ). Then, variations of temperature and of the constants that characterise the nonlinear diffusion lead to slight modifications on the conduction velocity. Here this value is computed using the approximate potential and activation times measured between the points  $(x, y, z) = (2.69, 1.68, 1.68)$  and  $(x, y, z) = (2.016, 1.68, 1.68)$ , that is a spatial variation in the  $x$ -direction of  $\delta x = 0.674$  cm, and employing a threshold of amplitude

1. We also vary the mesh resolution and observe that the coarsest spatio-temporal discretisation that maintains conduction velocities in physiological ranges requires a meshsize of  $h = 0.28$  and a timestep of  $\Delta t = 0.3$  ms. Our results are summarised in Table 4.2. We can note that for the lowest temperatures, the changes in resolution entail substantial modifications in the conduction velocity, whereas for the highest temperatures the effect seems to be milder and even coarse meshes give physiological results. After computing each conduction velocity value, we have commenced another pacing cycle and run the simulation until  $t = 120$  ms. Snapshots of the potential, recovery, cell shortening, and solid pressure are depicted in Figure 4.1, where we can observe a marked deformation on the sheetlet direction complying with the shortening in the fibre direction.

Table 4.2: Computed conduction velocities according to different temperature values and spatio-temporal refinement. The values of the space parameter are in cm and the timesteps in ms.

Temperature	$h = 0.28, \Delta t = 0.3$	$h = 0.14, \Delta t = 0.075$	$h = 0.07, \Delta t = 0.0125$
$T = 33^\circ\text{C}$	0.326	0.345	0.388
$T = 35^\circ\text{C}$	0.392	0.397	0.403
$T = 37^\circ\text{C}$	0.402	0.411	0.414
$T = 39^\circ\text{C}$	0.405	0.409	0.411
$T = 41^\circ\text{C}$	0.405	0.410	0.412

## 4.2 Scroll wave dynamics and localised temperature gradients

We now perform a series of tests aimed at analysing the differences in wave propagation patterns produced with different temperature conditions. First on the case of the base temperature  $T = 37^\circ\text{C}$ , secondly in the case where the domain is subject to a temperature gradient in the direction of the sheetlets  $\mathbf{s}_0 = (0, 1, 0)^\text{t}$ , and third when the temperature has a radial gradient in the  $xy$  plane; that is

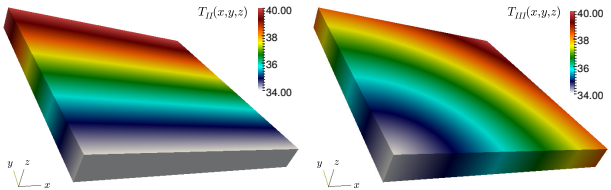
$$\begin{aligned}
 T_{II}(x, y, z) &= \frac{1}{6.72}(40^\circ\text{C}y + 34^\circ\text{C}(6.72 - y)), \\
 T_{III}(x, y, z) &= \frac{1}{R}(40^\circ\text{C}r + 34^\circ\text{C}(R - r)), \\
 r &= (x^2 + y^2)^{1/2}, \quad R = 6.72\sqrt{2}.
 \end{aligned}$$


Figure 4.2: Temperature distributions in the undeformed configuration, where the colour code is in  $^\circ\text{C}$ .

The domain of interest is now the slab  $\Omega = (0, 6.72) \times (0, 6.72) \times (0, 0.672)$ , which we discretise into a structured mesh of 72000 tetrahedral elements. We use a fixed timestep  $\Delta t = 0.3$  ms and set a constant fibre direction  $\mathbf{f}_0 = (1, 0, 0)^\text{t}$ . We employ a S1-S2 protocol to initiate scroll waves [3], where S1 is a square wave stimulation current of amplitude 3 and duration 3 ms, starting at  $t = 1$  ms on the face defined by  $x = 0$ ; and S2 is a step function of the same duration and amplitude, applied on the lower left octant of the domain at  $t = 350$  ms. This time the boundary conditions for the structural problem are precisely as in (2.11), using the constant  $\eta = 0.05$ ; and the boundary conditions for the electrophysiology adopt the form (2.12). Figure 4.3 shows two snapshots of the voltage propagation through the deformed tissue slab for the first case, of constant temperature (case I). Differences between the patterns obtained at different temperatures are qualitatively shown in Figure 4.4, which displays the difference in the potential between case II and case I, as well as between case III and case I. A fourth case (not shown) was also tested, where the temperature gradient is placed in the direction



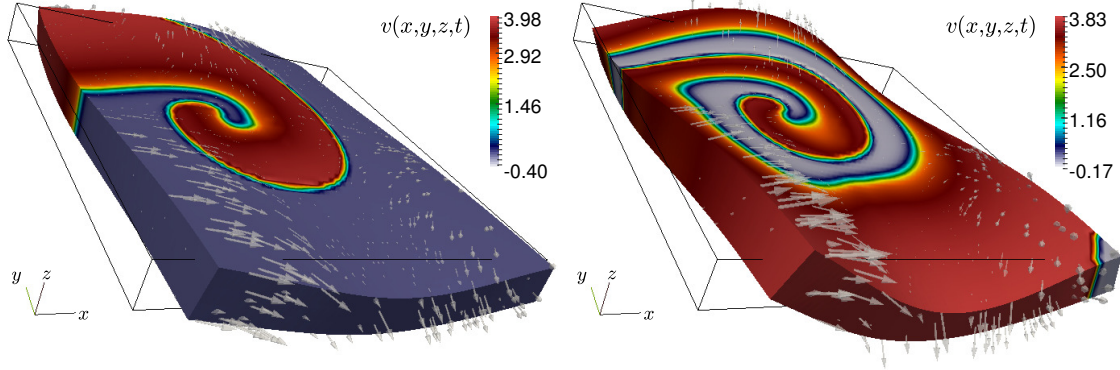


Figure 4.3: Scroll waves developed after  $t = 450$  ms and  $t = 600$  ms using  $T = 37^\circ\text{C}$ , plotted on the deformed configuration, and where arrows indicate displacement directions.

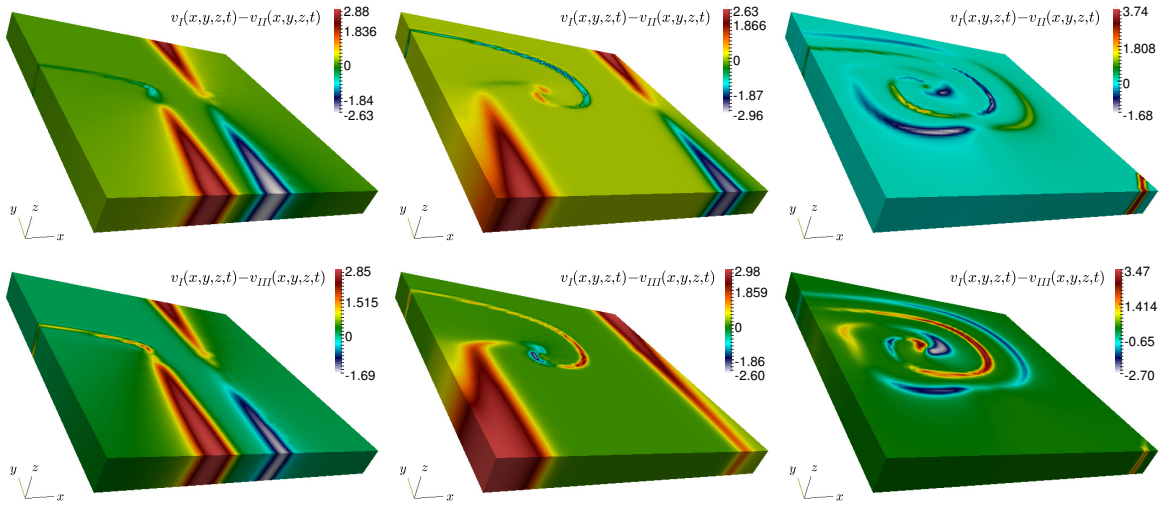


Figure 4.4: Potential difference between case I (uniform temperature at  $T = 37^\circ\text{C}$ ) and two different gradient distributions in the sheetlet (case II - top) and radial directions (case III - bottom), plotted on the reference domain at times  $t = 350, 450, 600$  ms.

of the fibres. Then the differences in propagation are much more pronounced (up to the point that the S1-S2 protocol described above is not able to produce scroll waves).

### 4.3 Scroll waves in an idealised left-ventricular geometry

We generate the geometry of a truncated ellipsoid and unstructured tetrahedral meshes using GMSH [22]. The domain has a height (base-to-apex) of 6.8 cm, a maximal equatorial diameter of 6.6 cm, a ventricular thickness of 0.5 cm at the apex and of 1.3 cm at the equator. Relatively coarse and fine partitions with 10793 and 83090 elements are used for the simulations in this subsection. Consistently with other electromechanical simulations on idealised ventricular geometries, here we consider a time-dependent pressure distributed uniformly on the endocardium (that is, using the second relation in (2.10)). In addition, on the basal cut we impose zero normal displacements (the first condition in (2.10)), and on the epicardium we impose Robin conditions (2.11) setting a spatially varying stiffness

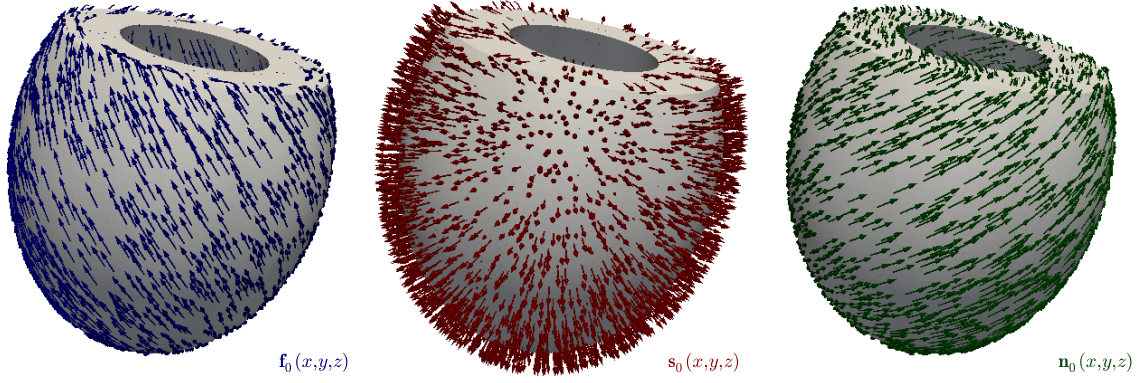


Figure 4.5: Fibres, radially-oriented sheetlets, and normal-sheetlet directions generated with a rule-based algorithm and employing  $\theta_{\text{epi}} = -50^\circ$ ,  $\theta_{\text{endo}} = 60^\circ$ .

coefficient, going linearly from  $\eta_{\text{max}}$  on the apex, to  $\eta_{\text{min}}$  on the base  $\eta(y) := \frac{1}{y_b - y_a} [\eta_{\text{max}}(y - y_b) + \eta_{\text{min}}(y - y_a)]$ , where  $y_a, y_b$  denote the vertical component of the positions at the apex and base, respectively. This strategy mimics the presence of the pericardial sac (as well as the combined elastic effect of other surrounding organs) having higher stiffness near the apex.

Fibre and sheetlet directions are constructed using a slight modification to the rule-based algorithm proposed in [48], that we outline here for the sake of completeness. The needed inputs are a unit vector  $\mathbf{k}_0$  aligned with the centreline and pointing from apex to base, the desired maximal and minimal angles that will determine the rotational anisotropy from epicardium to endocardium,  $\theta_{\text{epi}}, \theta_{\text{endo}}$ ; and boundary labels for the epicardium  $\partial\Omega_{\text{epi}}$ , endocardium  $\partial\Omega_{\text{endo}}$ , and basal cut  $\partial\Omega_{\text{base}}$ . The first step consists in solving the following Poisson problem (here stated in mixed form for a potential  $\phi$  and a preliminary sheetlet direction  $\zeta$ ) endowed with mixed boundary conditions

$$\begin{aligned} -\nabla \cdot \zeta &= 0 \quad \text{and} \quad \zeta = \nabla \phi \quad \text{in } \Omega, \\ \zeta \cdot \nu &= 0 \quad \text{on } \partial\Omega_{\text{base}}, \quad \phi = 0 \quad \text{on } \partial\Omega_{\text{endo}}, \quad \phi = 1 \quad \text{on } \partial\Omega_{\text{epi}}. \end{aligned}$$

The unknowns of this problem are discretised with Brezzi-Douglas-Marini elements of first order and piecewise constant elements [21]. Once a discrete first sheetlet direction  $\zeta_h$  is computed, the final sheetlet directions are obtained by normalisation  $\mathbf{s}_0 = \zeta_h / \|\zeta_h\|$ . Secondly, we project the centreline  $\widehat{\mathbf{k}}_0 = \mathbf{k}_0 - (\mathbf{k}_0 \cdot \mathbf{s}_0)\mathbf{s}_0$  and then compute a so-called flat fibre field using the sheetlet and the projected centreline vectors  $\widehat{\mathbf{f}}_0 = \mathbf{s}_0 \times \widehat{\mathbf{k}}_0 / \|\widehat{\mathbf{k}}_0\|$ . Thirdly, we proceed to project now the flat fibres onto the sheetlet planes exploiting the rotational anisotropy, through the operation

$$\widetilde{\mathbf{f}}_0 = \widehat{\mathbf{f}}_0 \cos(\theta(\phi_h)) + \mathbf{s}_0 \times \widehat{\mathbf{f}}_0 \sin(\theta(\phi_h)) + \mathbf{s}_0(\mathbf{s}_0 \cdot \widehat{\mathbf{f}}_0)[1 - \cos(\theta(\phi_h))],$$

where  $\phi_h$  is the discrete potential and the function  $\theta(\phi_h) := \frac{1}{180\pi} [(\theta_{\text{epi}} - \theta_{\text{endo}})\phi_h + \theta_{\text{endo}}]$  modulates the intramural angle variation. Finally, the fibres are recovered from normalising the projected field  $\mathbf{f}_0 = \widetilde{\mathbf{f}}_0 / \|\widetilde{\mathbf{f}}_0\|$  (all normalisations in this Section refer to component-wise operations using the Euclidean norm). Sample fibre, sheet and normal directions generated using this algorithm are shown in Figure 4.5.

The additional constants employed in this Section are  $\theta_{\text{epi}} = -50^\circ$ ,  $\theta_{\text{endo}} = 60^\circ$ ,  $\eta_{\text{max}} = 0.6 \text{ kPa}$  (that is, we consider a transmurally asymmetric fibre distribution), and  $\eta_{\text{min}} = 0.001 \text{ kPa}$ . As in the tests reported in previous subsections, the dynamics here are initiated through an S1-S2 approach, where the first wave is set on the apex and the second wave is initiated at the same location, but only for the quadrant  $x > 0, z > 0$ . Until the two main waves are formed, we do not initiate the coupling

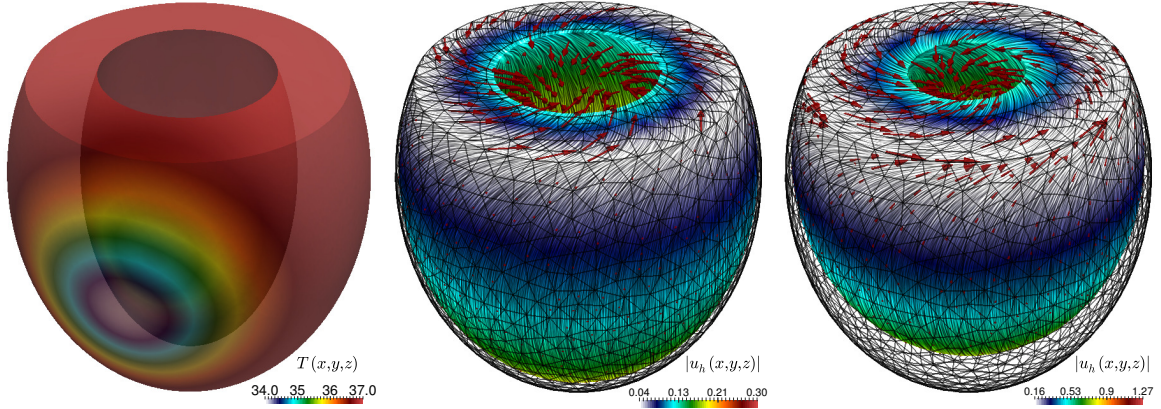


Figure 4.6: Temperature distribution for the second test case (left), and two snapshots illustrating the torsion and wall-thickening of the left ventricle (the arrows indicate the displacement direction).

with the active mechanics. We consider two cases: one when the temperature is kept constant at  $37^\circ\text{C}$ , and another when at the time of switching on the electromechanical coupling, a localised point in the upper epicardium is maintained at a lower temperature  $34^\circ\text{C}$ . The temperature distribution in this second case is defined as  $T(x, y, z) = 37 - 3 \exp(-[(x - 3)^3 + y^2 + z^2]/3)$  (see the leftmost panel in Figure 4.6). We illustrate the torsion and wall-thickening effects achieved by the orthotropic activation model in the centre and right panels of Figure 4.6.

Finally, a few snapshots of the scroll wave dynamics for the two cases are presented in Figure 4.7, indicating again an important model dependency on temperature variations. Further investigations are necessary to determine the potential effects of the thermal coupling into the formation of pinning or unpinning, and also the influence of the mechanochemical patterns in the modification of alternans.

## 5 Concluding remarks

We have advanced a new theoretical framework for the modelling of cardiac electromechanics that incorporates active strain, nonlinear diffusion, and thermo-electrical coupling as main ingredients. In addition we have performed a preliminary computational study that addresses the influence of space and time discretisation resolutions at different thermal states in a idealised three-dimensional domain. Comparisons were made in terms of conduction velocity values as well as onset and development of scroll wave dynamics as precursors of life threatening arrhythmias.

Naturally, many generalisations and improvements are envisaged at this stage. First, the inclusion of higher complexity in the electrophysiology and in the contraction models can be readily done without modifying the basic structure of the coupling mechanisms, and they could lead to more refined conclusions regarding the control of arrhythmias and fibrillation. Secondly, it is left to investigate whether spatio-temporal variations of temperature have an effect, perhaps in long term and operating theatre scenarios. In perspective, the present study could serve in understanding and possibly controlling temperature-altered cardiac dynamics in patients subjected to whole-body hyperthermia. This is a medical procedure relevant for treating metastatic cancer and severe viral infections as e.g. HIV [30, 34]. In addition, we foresee the application of the present model and computational methodology into the study of spatio-temporal alternans [6, 17] as well as spiral pinning and unpinning phenomena [8, 28]. These supplementary studies would also contribute to further validate the proposed multiphysics framework against experimental evidence. In fact, the idealised ventricular domain embedded with myocardial fibres in rotational anisotropy that we used in Section 4.3 can be

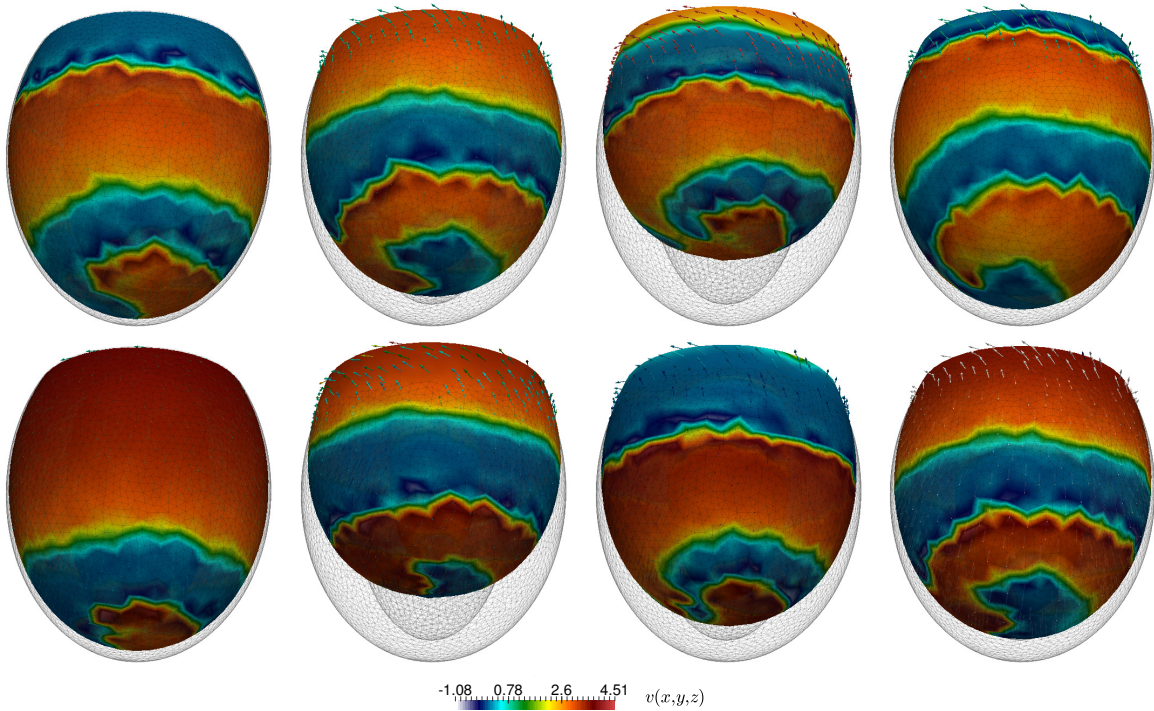


Figure 4.7: Propagation of the transmembrane potential plotted on the deformed domain, using a constant temperature (top panels) and a cold spot (bottom).

readily exploited towards the characterisation of the unknown intramural dynamics. A further tuning of the material parameters using synchronised endocardial and epicardial optical mapping datasets will also be carried out.

We close this section pointing out a few possible extensions to this model that do not require extensive validation nor physiologically detailed descriptions. First, the passive material properties of the muscle have been considered independent of temperature, and a simple constitutive relation could be embedded in the strain-stress law using the results from [53], or in the cell contraction model following e.g. [39, 55]. Secondly, time-dependent mechanobiology stability [16], together with growth and remodelling effects [14, 15, 38] could be incorporated in the present framework considering distributed properties of collagen and muscular fibres, following for instance [43]. Mechanoelectric feedback has been left out from this study (with the aim of isolating the effects of the thermo-electric contribution in an electromechanical context), so we could readily employ recent models for stretch activated currents [47, 56], or alternatively employ stress-assisted conductivity as in [9]. Other extensions include the use of geometrically detailed biventricular meshes, more sophisticated boundary conditions (setting for instance pressure-volume loops on the endocardium), and the presence of Purkinje networks [13] and/or fast conduction systems that could definitely have an impact on the reentry dynamics. Goals in the longer term deal with optimal control problems exploiting data assimilation techniques using imaging tools and *in silico* testing of novel defibrillation protocols [40].

## Acknowledgments

Fruitful discussions with Daniel E. Hurtado (PUC), Francesc Levrero (Oxford), Simone Pezzuto (USI), and Simone Rossi (Duke) are gratefully acknowledged. This work has been partially supported by the

Italian National Group of Mathematical Physics (GNFM-INdAM), by the International Center for Relativistic Astrophysics Network (ICRANet), and by the Engineering and Physical Sciences Research Council (EPSRC) through the research grant EP/R00207X/1.

## References

- [1] M. S. ALNÆS, J. BLECHTA, J. HAKE, A. JOHANSSON, B. KEHLET, A. LOGG, C. RICHARDSON, J. RING, M. E. ROGNES, AND G. N. WELLS, *The FEniCS project version 1.5*, Archive of Numerical Software, 3 (2015), pp. 9–23.
- [2] D. BINI, C. CHERUBINI, AND S. FILIPPI, *On vortices heating biological excitable media*, Chaos Solitons & Fractals, 42 (2009), pp. 2057–2066.
- [3] D. BINI, C. CHERUBINI, S. FILIPPI, A. GIZZI, AND P. E. RICCI, *On spiral waves arising in natural systems*, Communications in Computational Physics, 8 (2010), p. 610.
- [4] D. BRAESS AND P. MING, *A finite element method for nearly incompressible elasticity problems*, Mathematics of Computation, 74 (2005), pp. 25–52.
- [5] K. S. CHAVAN, B. P. LAMICHHANE, AND B. I. WOHLMUTH, *Locking-free finite element methods for linear and nonlinear elasticity in 2D and 3D*, Computer Methods in Applied Mechanics and Engineering, 196 (2007), pp. 4075–4086.
- [6] D. D. CHEN, R. A. GRAY, I. UZELAC, C. HERNDON, AND F. H. FENTON, *Mechanism for amplitude alternans in electrocardiograms and the initiation of spatiotemporal chaos*, Physical Review Letters, 118 (2017), p. 168101.
- [7] E. M. CHERRY AND F. H. FENTON, *Effects of boundaries and geometry on the spatial distribution of action potential duration in cardiac tissue*, Journal of Theoretical Biology, 285 (2011), pp. 164–176.
- [8] C. CHERUBINI, S. FILIPPI, AND A. GIZZI, *Electroelastic unpinning of rotating vortices in biological excitable media*, Physical Review E, 85 (2012), p. 031915.
- [9] C. CHERUBINI, S. FILIPPI, A. GIZZI, AND R. RUIZ-BAIER, *A note on stress-driven anisotropic diffusion and its role in active deformable media*, Journal of Theoretical Biology, 430 (2017), pp. 221–228.
- [10] A. COLLET, J. BRAGARD, AND P. C. DAUBY, *Temperature, geometry, and bifurcations in the numerical modeling of the cardiac mechano-electric feedback*, Chaos: An Interdisciplinary Journal of Nonlinear Science, 27 (2017), p. 093924.
- [11] P. COLLI FRANZONE, L. F. PAVARINO, AND S. SCACCHI, *Bioelectrical effects of mechanical feedbacks in a strongly coupled cardiac electro-mechanical model*, Mathematical Models and Methods in Applied Sciences, 26 (2016), pp. 27–57.
- [12] F. S. COSTABAL, F. A. CONCHA, D. E. HURTADO, AND E. KUHL, *The importance of mechano-electrical feedback and inertia in cardiac electromechanics*, Computer Methods in Applied Mechanics and Engineering, 320 (2017), pp. 352–368.
- [13] F. S. COSTABAL, D. E. HURTADO, AND E. KUHL, *Generating purkinje networks in the human heart*, Journal of Biomechanics, 49 (2016), pp. 2455–2465.
- [14] C. J. CYRON, R. C. AYDIN, AND J. D. HUMPHREY, *A homogenized constrained mixture (and mechanical analog) model for growth and remodeling of soft tissue*, Biomechanical Modeling in Mechanobiology, 15 (2016), pp. 1389–1403.

- [15] C. J. CYRON AND J. D. HUMPHREY, *Growth and remodeling of load-bearing biological soft tissues*, *Meccanica*, 52 (2017), pp. 645–664.
- [16] C. J. CYRON, J. S. WILSON, AND J. D. HUMPHREY, *Mechanobiological stability: a new paradigm to understand the enlargement of aneurysms?*, *Journal of the Royal Society Interface*, 11 (2014), p. 20140680.
- [17] M. DUPRAZ, S. FILIPPI, A. GIZZI, A. QUARTERONI, AND R. RUIZ-BAIER, *Finite element and finite volume-element simulation of pseudo-ECGs and cardiac alternans*, *Mathematical Methods in the Applied Sciences*, 38 (2015), pp. 1046–1058.
- [18] D. A. EISNER, J. L. CALDWELL, K. KISTAMÁS, AND A. W. TRAFFORD, *Calcium and excitation-contraction coupling in the heart*, *Circulation Research*, 121 (2017), pp. 181–195.
- [19] F. H. FENTON, A. GIZZI, C. CHERUBINI, N. POMELLA, AND S. FILIPPI, *Role of temperature on nonlinear cardiac dynamics*, *Physical Review E*, 87 (2013), p. 042709.
- [20] S. FILIPPI, A. GIZZI, C. CHERUBINI, S. LUTHER, AND F. H. FENTON, *Mechanistic insights into hypothermic ventricular fibrillation: the role of temperature and tissue size*, *Europace*, 16 (2014), pp. 424–434.
- [21] G. N. GATICA, *A Simple Introduction to the Mixed Finite Element Method. Theory and Applications*, Springer-Verlag, Berlin, 2014.
- [22] C. GEUZAIN AND J.-F. REMACLE, *Gmsh: A 3-D finite element mesh generator with built-in pre- and post-processing facilities*, *International Journal for Numerical Methods in Engineering*, 79 (2009), pp. 1309 – 1331.
- [23] A. GIZZI, C. CHERUBINI, S. FILIPPI, AND A. PANDOLFI, *Theoretical and numerical modeling of nonlinear electromechanics with applications to biological active media*, *Communications in Computational Physics*, 17 (2015), pp. 93–126.
- [24] A. GIZZI, C. CHERUBINI, S. MIGLIORI, R. ALLONI, R. PORTUESI, AND S. FILIPPI, *On the electrical intestine turbulence induced by temperature changes*, *Physical Biology*, 7 (2010), p. 016011.
- [25] A. GIZZI, A. LOPPINI, R. RUIZ-BAIER, A. IPPOLITO, A. CAMASSA, A. LA CAMERA, E. EMMI, L. DI PERNA, V. GAROFALO, C. CHERUBINI, AND S. FILIPPI, *Nonlinear diffusion & thermo-electric coupling in a two-variable model of cardiac action potential*, *Chaos: An Interdisciplinary Journal of Nonlinear Science*, 27 (2017), p. 093919.
- [26] A. V. HILL AND R. S. SEC, *The heat of shortening and the dynamic constants of muscle*, *Proceedings of the Royal Society of London B: Biological Sciences*, 126 (1938), pp. 136–195.
- [27] G. A. HOLZAPFEL AND R. W. OGDEN, *Constitutive modelling of passive myocardium: a structurally based framework for material characterization*, *Philosophical Transactions of the Royal Society of London A: Mathematical, Physical and Engineering Sciences*, 367 (2009), pp. 3445–3475.
- [28] M. HÖRNING, *Termination of pinned vortices by high-frequency wave trains in heartlike excitable media with anisotropic fiber orientation*, *Physical Review E*, 86 (2012), p. 031912.
- [29] D. E. HURTADO, S. CASTRO, AND A. GIZZI, *Computational modeling of non-linear diffusion in cardiac electrophysiology: A novel porous-medium approach*, *Computer Methods in Applied Mechanics and Engineering*, 300 (2016), pp. 70–83.
- [30] P. K. JHA, S. ANSHARMA AND R. MALVIYA, *Hyperthermia: Role and risk factor for cancer treatment*, *Achievements in the Life Sciences*, 10 (2016), pp. 161–167.

- [31] A. KARMA, *Electrical alternans and spiral wave breakup in cardiac tissue*, Chaos: An Interdisciplinary Journal of Nonlinear Science, 4 (1994), pp. 461–472.
- [32] ———, *Physics of cardiac arrhythmogenesis*, Annual Review of Condensed Matter Physics, 4 (2013), pp. 313–337.
- [33] R. KIENAST, M. HANDLER, M. STÖGER, D. BAUMGARTEN, F. HANSER, AND C. BAUMGARTNER, *Modeling hypothermia induced effects for the heterogeneous ventricular tissue from cellular level to the impact on the ecg*, PLOS ONE, 12 (2017), pp. 1–22.
- [34] D. N. KINSHT, *Modeling of heat transfer in whole-body hyperthermia*, Biophysics, 51 (2006), pp. 659–663.
- [35] S. LAND, S.-J. PARK-HOLOHAN, N. P. SMITH, C. G. DOS REMEDIOS, J. C. KENTISH, AND S. A. NIEDERER, *A model of cardiac contraction based on novel measurements of tension development in human cardiomyocytes*, Journal of Molecular and Cellular Cardiology, 106 (2017), pp. 68 – 83.
- [36] R. W. LAWTON, *The thermoelastic behavior of isolated aortic strips of the dog*, Circulation Research, 2 (1954), pp. 344–353.
- [37] J. LEE, S. NIEDERER, D. NORDSLETTEN, I. LE GRICE, B. SMAIL, D. KAY, AND N. SMITH, *Coupling contraction, excitation, ventricular and coronary blood flow across scale and physics in the heart*, Philosophical Transactions of the Royal Society of London A: Mathematical, Physical and Engineering Sciences, 367 (2009), pp. 2311–2331.
- [38] L. C. LEE, J. SUNDNES, M. GENET, J. F. WENK, AND S. T. WALL, *An integrated electromechanical-growth heart model for simulating cardiac therapies*, Biomechanical Modeling in Mechanobiology, 15 (2016).
- [39] X. LU, L. S. TOBACMAN, AND M. KAWAI, *Temperature-dependence of isometric tension and cross-bridge kinetics of cardiac muscle fibers reconstituted with a tropomyosin internal deletion mutant*, Biophysical Journal, 91 (2006), pp. 4230 – 4240.
- [40] S. LUTHER, F. H. FENTON, AND ET. AL., *Low-energy control of electrical turbulence in the heart*, Nature, 475 (2011), pp. 235–239.
- [41] M. P. NASH AND P. J. HUNTER, *Computational mechanics of the heart*, Journal of Elasticity, 61 (2000), pp. 113–141.
- [42] F. NOBILE, R. RUIZ-BAIER, AND A. QUARTERONI, *An active strain electromechanical model for cardiac tissue*, International Journal for Numerical Methods in Biomedical Engineering, 28 (2012), pp. 52–71.
- [43] A. PANDOLFI, A. GIZZI, AND M. VASTA, *Coupled electro-mechanical models of fiber-distributed active tissues*, Journal of Biomechanics, 49 (2016), pp. 2436–2444.
- [44] S. PEZZUTO, D. AMBROSI, AND A. QUARTERONI, *An orthotropic active-strain model for the myocardium mechanics and its numerical approximation*, European Journal of Mechanics - A/Solids, 48 (2014), pp. 83 – 96.
- [45] Z. QU, G. HU, A. GARFINKEL, AND J. N. WEISS, *Nonlinear and stochastic dynamics in the heart*, Physics Reports, 543 (2014), pp. 61–162.
- [46] A. QUARTERONI, T. LASSILA, S. ROSSI, AND R. RUIZ-BAIER, *Integrated heart – coupled multiscale and multiphysics models for the simulation of the cardiac function*, Computer Methods in Applied Mechanics and Engineering, 314 (2017), pp. 345–407.

- [47] T. A. QUINN, *Cardiac mechano-electric coupling: a role in regulating normal function of the heart?*, Cardiovascular Research, 108 (2015), pp. 1–3.
- [48] S. ROSSI, T. LASSILA, R. RUIZ-BAIER, A. SEQUEIRA, AND A. QUARTERONI, *Thermodynamically consistent orthotropic activation model capturing ventricular systolic wall thickening in cardiac electromechanics*, European Journal of Mechanics: A/Solids, 48 (2014), pp. 129–142.
- [49] S. ROSSI, R. RUIZ-BAIER, L. PAVARINO, AND A. QUARTERONI, *Orthotropic active strain models for the numerical simulation of cardiac biomechanics*, International Journal for Numerical Methods in Biomedical Engineering, 28 (2012), pp. 761–788.
- [50] R. RUIZ-BAIER, *Primal-mixed formulations for reaction-diffusion systems on deforming domains*, Journal of Computational Physics, 299 (2015), pp. 320–338.
- [51] A. J. M. SPENCER, *Continuum Mechanics*, Longman Group Ltd, London, 1989.
- [52] H. SUGI AND G. H. POLLACK, *Mechanisms of work production and work absorption in muscle*, vol. Advances in Experimental Medicine and Biology, Springer, 1998.
- [53] G. H. TEMPLETON, K. WILDENTHAL, J. T. WILLERSON, AND W. C. REARDON, *Influence of temperature on the mechanical properties of cardiac muscle*, Circulation Research, 34 (1974), pp. 624–634.
- [54] N. A. TRAYANOVA AND J. J. RICE, *Cardiac electromechanical models: from cell to organ*, Frontiers in Physiology, 2 (2011), p. 43.
- [55] G. WANG AND M. KAWAI, *Effect of temperature on elementary steps of the cross-bridge cycle in rabbit soleus slow-twitch muscle fibres*, The Journal of Physiology, 531 (2001), pp. 219–234.
- [56] M.-L. WARD, I. A. WILLIAMS, I. CHU, P. J. COOPER, Y. K. JU, AND D. G. ALLEN, *Stretch-activated channels in the heart: Contributions to length-dependence and to cardiomyopathy*, Progress in Biophysics and Molecular Biology, 97 (2008), pp. 232–249.
- [57] T. E. WILSON AND C. G. CRANDALL, *Effect of thermal stress on cardiac function*, Exercise and Sport Sciences Reviews, 39 (2011), pp. 12–17.